# Fast Prediction of Two-Dimensional Flowfields with Fuel Injection into Supersonic Crossflow via Deep Learning

AKIYAMA, Kento
Department of Aeronautics and Astronautics, Kyushu University

OGAWA, Hideaki
Department of Aeronautics and Astronautics, Kyushu University

https://hdl.handle.net/2324/7172135

出版情報：Transactions of the Japan Society for Aeronautical and Space Sciences. 66 (5), pp.164-173, 2023-09-04. 日本航空宇宙学会
バージョン：

Trans. Japan Soc. Aero. Space Sci.
Vol. 66, No. 5, pp. 164–173, 2023
DOI: 10.2322/tjsass.66.164

# Fast Prediction of Two-Dimensional Flowfields with Fuel Injection into Supersonic Crossflow via Deep Learning*

Kento AKIYAMA and Hideaki OGAWA†

*Department of Aeronautics and Astronautics, Kyushu University, Fukuoka 819–0395, Japan*

Fuel injection is one of the most crucial components for scramjet engines, a promising hypersonic airbreathing technology for economical and flexible space transportation systems. While surrogate modeling based on machine learning has been employed to replace computational simulations for performance evaluation in design optimization of such components, it can inherently predict performance parameters only as scalar quantities. This study investigates the capability of deep learning to predict the fuel injection flowfields, aiming to assist with data-driven approaches for data mining and optimization. Two-dimensional flowfields with sonic fuel injection into a Mach 3.8 crossflow have been trained using the multilayer perceptron. The resultant model has been found to be able to predict the flowfields instantaneously with reasonable accuracy. Local sensitivity analysis has been performed to examine the influence of the design variables on flow properties to gain insights into the effects of their variations on local flow phenomena.

**Key Words:** Deep Learning, Computational Fluid Dynamics, Compressible Flows, Fuel Injection, Scramjet Propulsion

## Nomenclature

$b$: bias in neural network
$c$: mass fraction
$f$: activation function
$f_n$: output of neural network
$h$: output of hidden layer
$H$: height of computational domain, m
$L$: distance to centerline of injector, m
$M$: Mach number
$p$: static pressure, Pa
$p_j$: injection pressure, Pa
$R^2$: coefficient of determination
$S$: distance to exit of domain, m
$S_f$: sensitivity of output to input
$t$: true value
$T$: static temperature, K
$U$: streamwise velocity component, m/s
$V$: vertical velocity component, m/s
$w$: weight in neural network
$w_j$: injection width, m
$x$: streamwise coordinate, m
$x_i$: input variable to neural network
$x^*$: standardized value
$y$: vertical coordinate, m
$\hat{y}$: prediction value
$y^+$: non-dimensional wall distance
$\alpha_j$: injection angle, deg
$\mu$: mean value
$\sigma$: standard deviation

Subscripts

$\infty$: freestream
j: fuel injection



*Presented at the 33rd International Symposium on Space Technology and Science, 26 February–4 March 2022, Beppu, Japan.
Received 25 October 2022; final revision received 6 February 2023; accepted for publication 22 March 2023.
†Corresponding author, hideaki.ogawa@aero.kyushu-u.ac.jp

## 1. Introduction

Hypersonic airbreathing propulsion offers the potential to enable a reliable and economical means of transportation for access to space and high-speed atmospheric flight. In particular, supersonic combustion ramjet (scramjet) engines are a promising technology that can realize efficient and flexible transportation systems by removing the limitations of conventional rockets engines, including the need to carry oxidizers. Continuous efforts dedicated to scramjets have led to various flight experiments.[1,2)]

Fuel injection is one of the key components for scramjet engines; characterized by an extremely short time scale and complex interactions between fuel and air, including mixing, ignition, and combustion. The development of an effective and reliable fuel-injection system is thus of crucial importance for successful scramjet operation. Numerous experimental and numerical studies have been conducted to investigate the characteristics of flowfields for transverse injection into supersonic flow.[3–6)]

Fuel injection for supersonic combustion commonly aims to maximize mixing efficiency and total pressure savings, while ensuring desirable penetration to achieve reliable and efficient scramjet operation. Effective design approaches to fulfill such multiple design requirements include methodologies that combine computational fluid dynamics (CFD) and multi-objective design optimization (MDO) using population-based algorithms such as evolutionary algorithms. Despite their ability for robust search, such approaches inherently require large computational cost to identify the Pareto optimal front comprising non-dominated solutions in the design space based on evaluations of individuals in the population pool. Surrogate modeling based on machine learning has been developed to be incorporated into the MDO framework so as to mitigate the computational cost. MDO frameworks assisted by surrogate modeling have been applied successfully to various design optimization problems for scramjet components.[7,8] However, conventional surrogate models can generally predict only scalar functions, and thus do not provide information on local flowfields. It is therefore difficult to gain insights into relations between performance and physical phenomena directly without performing CFD simulations and probing into the results for selected solutions. To overcome this limitation of such approaches, reduced order modeling techniques such as proper orthogonal decomposition and dynamic mode decomposition are utilized owing to their ability to decompose and reconstruct flowfields.[9,10]

With the recent advancement of computing technologies, the field of data science has further advanced, paving the way for state-of-the-art data-driven approaches. In particular, deep learning can represent complex functions flexibly and accurately, as compared to conventional methods. Its capability has successfully been demonstrated in a wide range of domains such as image processing, automated driving, and medicine. Deep learning has also been applied to various problems in the fields of fluid dynamics and fluid engineering including feature extraction[11] and physics-informed neural networks.[12,13] Sekar et al. investigated the capability of deep learning approaches to predict the flowfields around airfoils by utilizing a convolutional neural network (CNN) and multilayer perceptron (MLP), and verified the ability to accurately predict the flowfields even for geometries that have not been used for training.[14] In the research of scramjet engines, Kong et al. utilized a CNN to predict the velocity flowfields from measured wall pressure in scramjet isolators, verifying the accuracy of the prediction.[15] However, deep learning has not been applied to supersonic jet-to-crossflow flowfields caused by scramjet fuel injection, despite significant benefits to be brought by the fast prediction of such complex flowfields in scramjet combustor design. Furthermore, no preceding work has discussed the utility of automatic differentiation from deep learning for local sensitivity analysis, which can be used to predict the behavior of local flow phenomena in response to changes in the design conditions.

The present study investigates the capability of a deep learning-based approach to predict complex flowfields caused by transverse gas injection into a supersonic crossflow, aiming to enable an advanced MDO framework incorporating multi-dimensional data-driven approaches. Two-dimensional jet-to-crossflow flowfields with two design variables, namely injection pressure and angle, are calculated by solving the compressible Navier-Stokes equations to generate a dataset. Upon training via MLP, the resultant model is tested for the flowfields that have not been used in training to assess its performance and robustness. In addition, local sensitivity analysis is performed to allow for detailed investigation of the influence of the design variables on local flow properties.

## 2. Approaches

### 2.1. Setups

#### 2.1.1. Flow condition

The freestream conditions are Mach number $M_\infty = 3.76$, static pressure $p_\infty = 1.03 \times 10^5$ Pa, and static temperature $T_\infty = 74.4$ K. Helium at a static temperature of $T_\mathrm{j} = 214.1$ K is used as the fuel to allow the investigation of flowfields caused by fuel/air mixing without combustion as well as comparison with the experiment conducted by Inoue et al.[16] It is injected sonically into the freestream airflow at a Mach number of $M_\mathrm{j} = 1.0$. The air composed of oxygen and nitrogen and helium are both assumed as calorically perfect gases with constant specific heat ratios.

#### 2.1.2. Configuration

The configuration of the injector and the flow domain is shown in Fig. 1, along with the computational mesh and boundary conditions. It schematically displays two main parameters; namely, the injection pressure $p_\mathrm{j}$ and the injection angle $\alpha_\mathrm{j}$. The injection width $w_\mathrm{j}$ is determined according to the injection pressure to supply the fuel (helium) so as to ensure a constant mass flow rate. A separate CFD computation is performed on a flat plate over a distance of 240 mm to obtain the flow profile for the turbulent boundary layer to be imposed at the entrance of the computational domain. In the current study, the origin of the domain is set at the center of the injection. The height of the computational domain ($H$), the distance from the leading-edge to the centerline of the injection ($L$), and that from the centerline of the injection to the exit of the computational domain ($S$) are fixed at 100 mm, 60 mm, and 100 mm, respectively.

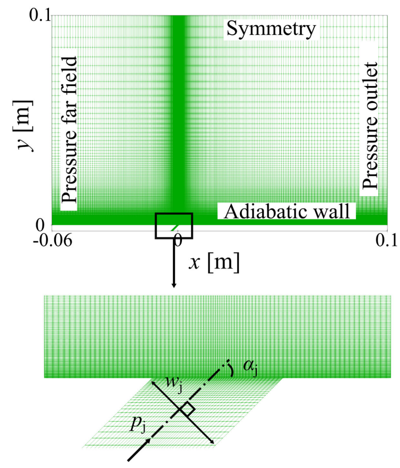


Fig. 1. Computational mesh and boundary conditions. (Top: overall domain, Bottom: close-up view)

## 2.2. Computational fluid dynamics

### 2.2.1. Numerical scheme

The steady injection flowfield is computed by solving the Reynolds-averaged Navier-Stokes (RANS) equations using the commercial CFD solver ANSYS Fluent 2021 R1.[17] The computation is performed at the second-order spatial accuracy, with the Advection Upstream Splitting Method (AUSM)[18] utilized for flux splitting and the SST $k$-$\omega$ model[19] for turbulence modeling. The convergence is assessed based on the energy residual (i.e., criterion set at $10^{-3}$ in the present study) as well as the difference between the inflow and outflow mass flow rates, the latter of which needs to be less than $10^{-3}$ kg/s·m, and is equivalent to $3.2 \times 10^{-3}$% of the inflow mass flow rate.

### 2.2.2. Computational mesh

The computational domain represented by a fully structured mesh is generated by an open-source mesh generator Gmsh.[20] The domain comprises 136,473 cells in total, with the height of the lowest cells fixed at 0.003 mm, which results in the value of the average nondimensional wall distance $y^+$ being less than 1.0.

### 2.2.3. Validation

A preliminary study is performed to examine the validity of the numerical modeling. Figure 2 compares the surface pressure distributions on the bottom wall between the present numerical (CFD) result and the experimental measurement reported in the preceding work.[16] That study also considered two-dimensional helium injection into a supersonic airstream with the same flow conditions at an injection pressure of $9.76 \times 10^4$ Pa and an injection angle of 90 deg. Reasonable agreement can be seen between them, validating the numerical setup used in this study.

### 2.2.4. Mesh sensitivity

A mesh sensitivity analysis is conducted to determine a suitable resolution capable of resolving the flowfield in adequate detail at a reasonable computational cost. The mesh consists of 66,280 cells for the coarse resolution, 136,473 cells for the medium resolution, and 498,830 cells for the fine resolution. Figure 3 compares the wall pressure distributions for each resolution, exhibiting rather little difference among all mesh resolutions. Based on this analysis, the medium mesh resolution is chosen to strike a balance between the computational cost and accuracy for the main study.

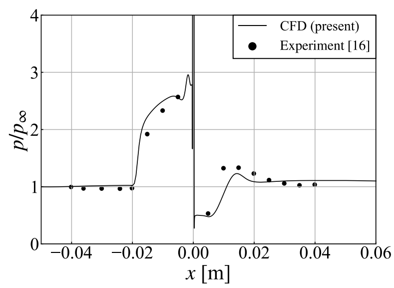


Fig. 2. Comparison of wall pressure distributions between present CFD and the preceding experiment.[16]

## 2.3. Deep learning

### 2.3.1. Multilayer perceptron

MLP is utilized for predicting jet-to-crossflow flowfields owing to its suitability to predict flow properties on arbitrary coordinates in the domain in the prospect of using the trained model for design optimization. Training and prediction using MLP are performed on NVIDIA TITAN RTX graphics cards featuring the Turing architecture with 4,608 CUDA cores and the Tensorflow 2.4.0 open-source library[21] at single precision. The MLP network architecture is shown in Fig. 4, consisting of input, hidden, and output layers. The input layer receives the user-defined input features, which are transformed using linear combination and a nonlinear activation function.

This transformation is applied to each layer up to the output layer, which returns the prediction results. The output of a neuron in the first hidden layer and that of the $l$th hidden layer are given by

$$h_j^1 = f_1\left(\sum_{k=1}^{4}\left(w_{jk}^1 x_k + b_j^1\right)\right) \tag{1}$$

$$h_j^l = f_l\left(\sum_{k=1}^{N^{l-1}}\left(w_{jk}^l h_k^{l-1} + b_j^l\right)\right) \tag{2}$$

where $x_k$ is the $k$th input, $N^{l-1}$ is the number of neurons for the $l-1$th layer, $h_k^l$ is the output from the $k$th neuron in the $l$th layer, $f$ is the nonlinear activation function, $w_{jk}$ is the weight from the $k$th neuron in the previous layer to the $j$th neuron of the current layer, and $b_j$ is the bias term in the $j$th neuron.

The coordinates $(x, y)$ and the design variables (i.e., injection pressure and injection angle) are used as the input vari-

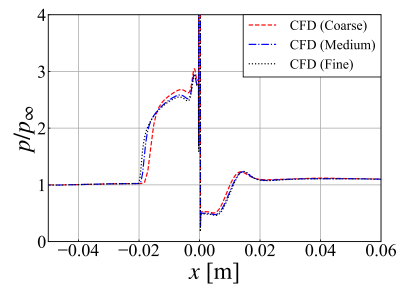


Fig. 3. Comparison of wall pressure distributions from CFD calculations using various mesh resolutions.

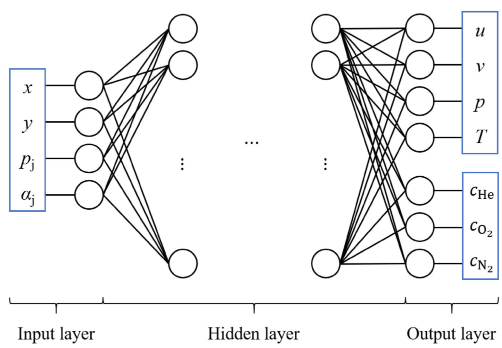


Fig. 4. MLP flow prediction network.

Table 1. Ranges of design variables.

| Design variable | Lower limit | Upper limit |
|---|---|---|
| Injection pressure $p_j$ [Pa] | 50,000 | 200,000 |
| Injection angle $\alpha_j$ [deg] | 30 | 90 |

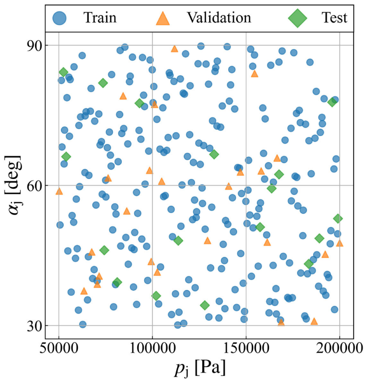


Fig. 5. Distributions of design variables.

ables. The flow properties, namely velocity components, static pressure, static temperature, mass fractions of helium, oxygen, and nitrogen, are predicted at each location. There are two output layers in this study; that is, one for mass fractions and the other for the other flow variables (i.e., velocity components, static pressure, and static temperature). To allow for prediction using the trained model and assessment of its performance with minimum tuning requirements, the rectified linear unit function (ReLU) and the Softmax function are utilized as the activation functions.[22] The latter is used only in the output layer of the mass fractions to ensure that the sum of the mass fractions is unity.

### 2.3.2. Sampling

Latin hypercube sampling (LHS) is utilized to generate the dataset quasi-uniformly without biasing.[23] Flowfields were calculated for 300 cases yielded by LHS: 292 satisfied the convergence criteria and were used to create an MLP model, 250 cases were used for training, 25 cases were used for validation, and the remainder for testing. As described in Section 2.1.2, the flowfield is defined by two design parameters; namely, injection pressure ($p_j$) and injection angle ($\alpha_j$) whose ranges are shown in Table 1. The distributions of these design variables in the design space are plotted in Fig. 5. Each flowfield has 137,255 nodes, thus the number of the training data points totals approximately 30 million.

### 2.3.3. Training

The training of MLP is performed using gradient-based optimization, utilizing back-propagation for calculation of the gradient of the loss function with respect to each weight and bias. In this study, the neural network consists of five fully connected layers comprising 500 neurons per layer. There are two output layers in the present study; hence, the loss function is expressed as

$$E = E_1 + E_2 \tag{3}$$

where $E_1$ is the loss function for the velocity components, static pressure, and static temperature, and $E_2$ is for the mass fractions. The mean squared error (MSE) loss function is utilized for $E_1$, whereas the MSE and categorical cross-entropy (CCE) loss function are considered for the mass fractions. The MSE and the CCE are defined by Eqs. (4) and (5), respectively:

Table 2. Setup of MLP training.

| | |
|---|---|
| Epochs | 150 |
| Optimizer | Adam |
| Learning rate | 0.0005 |
| Batch size | 4,096 |

$$L_1 = \frac{1}{NM}\sum_{i=1}^{N}\sum_{j=1}^{M}\left(\hat{y}_{i,j} - t_{i,j}\right)^2 \tag{4}$$

$$L_2 = -\frac{1}{NM}\sum_{i=1}^{N}\sum_{j=1}^{M} t_{i,j}\log\hat{y}_{i,j} \tag{5}$$

where $t$ is the true (actual) value (i.e., CFD), $\hat{y}$ is the predicted value, $N$ is the number of data points, and $M$ is the number of prediction variables. Adaptive momentum estimation (Adam)[24] is chosen as the activation function as it allows for the assessment of the MLP performance with minimum tuning requirements. It minimizes the loss function by applying the default hyperparameters (i.e., $\beta_1 = 0.9$, $\beta_2 = 0.999$, and $\varepsilon = 10^{-7}$).

Prior to training, standardization is applied to the input variables ($x$ and $y$ coordinates and design variables) and the flow properties except for the mass fractions (i.e., velocity components, static pressure, and static temperature) to scale the data to the same range. The standardization process is expressed as $x^* = (x - \mu)/\sigma$, where $x$ is the variable, $\mu$ is the mean value, and $\sigma$ the standard deviation. The details of the training setup are shown in Table 2.

### 2.3.4. Sensitivity analysis

Among the various approaches that have been proposed to interpret the behavior of deep learning models,[25,26] the gradient-based method,[27] where gradients are calculated to examine the influence of input variation on the prediction (i.e., output), is considered in this study. To investigate the local influence of the design variables on the flowfield, local sensitivity analysis is conducted to quantify the gradients for each node, defined as

$$S_f(x) = \frac{\partial f_n(x)}{\partial x_i} \tag{6}$$

where $f_n$ is the output of the neural network (MLP) and $x_i$ is the design variable (input). This calculation is performed utilizing automatic differentiation based on the chain rule performed during the training phase.[28]

## 3. Results

### 3.1. Training

Two loss functions (i.e., the mean squared loss ($L_1$) and the categorical cross-entropy loss ($L_2$)) are considered and calculated for the mass fractions. They are compared using root mean squared error (RMSE) defined as:

$$\mathrm{RMSE} = \sqrt{\frac{1}{N}\sum_{i=1}^{N}\left(\hat{y}_i - t_i\right)^2} \tag{7}$$

where $t$ is the true value (i.e., CFD), $\hat{y}$ is the predicted value, and $N$ is the number of data points. Figure 6 compares the RMSEs of these loss functions for the validation data. It should be noted that, while these two loss functions are considered only for mass fractions, the MLP model is also trained for predicting the velocity components, static temperature, static pressure, and mass fractions simultaneously. Figure 6 therefore shows the RMSEs of these properties that have been calculated from standardized values, as well as the training for prediction models as described in Section 2.3.3, in addition to those of mass fractions. It can be seen that the RMSEs for all target flow variables are smaller than the mean squared loss (MSE) when the categorical cross-entropy (CCE) loss is used. The CCE loss is therefore chosen for the following study.

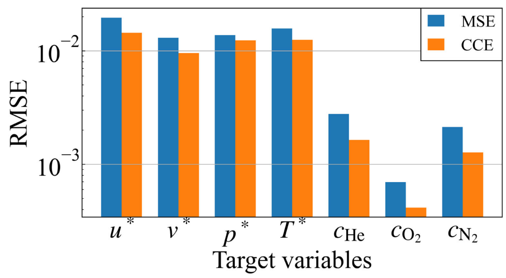


Fig. 6. Comparison of RMSEs between MSE loss function ($L_1$) and CCE loss function ($L_2$).

Figure 7 compares the values from CFD and prediction for all 17 test cases for each flow property. Also shown is the coefficient of determination $R^2$ defined as

$$R^2 = 1 - \frac{\sum_{i=1}^{N}\left(t_i - \hat{y}_i\right)^2}{\sum_{i=1}^{N}\left(t_i - \bar{t}\right)^2} \tag{8}$$

where $t$ is the true value (from CFD), $\bar{t}$ is the averaged true value, $\hat{y}$ is the predicted value, and $N$ is the number of data points. This coefficient ranges between 0.0 and 1.0 (i.e., the larger the value of $R^2$, the more accurate the prediction). The $R^2$ values are greater than 0.999 for all flow properties, indicative of accurate prediction. The perpendicular error distribution that exists at $u_{\mathrm{CFD}} = 0\,\mathrm{m/s}$ in Fig. 7 (a) is attributed to the sparsity of data points on the wall, where a no-slip condition is imposed. Table 3 presents the RMSE values as well as the values of the mean absolute percentage error (MAPE) defined as:

$$\mathrm{MAPE} = \sqrt{\frac{1}{N}\sum_{i=1}^{N}\left|\frac{\hat{y}_i - t_i}{t_i}\right|} \tag{9}$$

where $t$ is the true value (CFD), $\hat{y}$ is the predicted value, and $N$ is the number of data points. The MAPEs for velocity components and mass fractions show large values owing to the near-zero values in the CFD results. The RMPEs for static pressure and static temperature are below 0.01 (i.e., 1%), signifying that the trained model can predict the properties with reasonable accuracy.

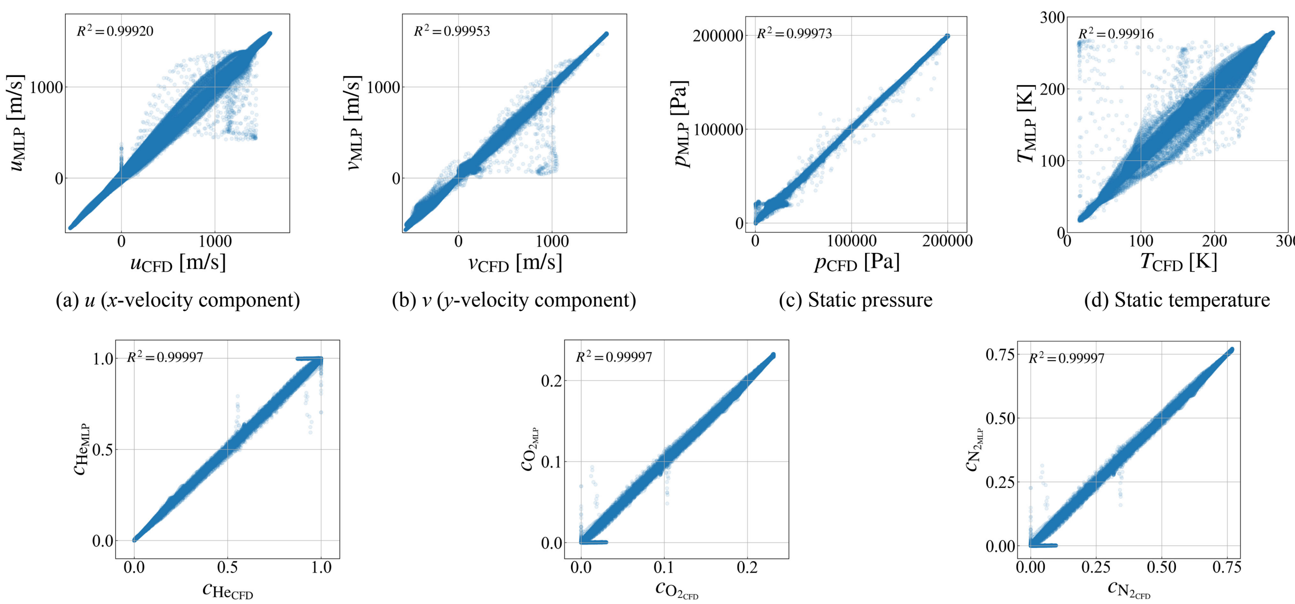


(a) $u$ ($x$-velocity component) (b) $v$ ($y$-velocity component) (c) Static pressure (d) Static temperature

(e) Helium mass fraction (f) Oxygen mass fraction (g) Nitrogen mass fraction

Fig. 7. Comparison between CFD and MLP results for all flow properties for all test cases.

Table 3. RMSE and MAPE values for all test cases.

| | $u$ [m/s] | $v$ [m/s] | $p$ [Pa] | $T$ [K] | $c_{\mathrm{He}}$ | $c_{\mathrm{O_2}}$ | $c_{\mathrm{N_2}}$ |
|---|---|---|---|---|---|---|---|
| RMSE | 11.4 | 7.16 | 306 | 2.22 | $25.0 \times 10^{-4}$ | $6.13 \times 10^{-4}$ | $19.2 \times 10^{-4}$ |
| MAPE | $4.52 \times 10^{6}$ | $4.52 \times 10^{6}$ | $8.90 \times 10^{-3}$ | $4.36 \times 10^{-3}$ | 1.91 | 7.52 | 18.9 |

### 3.2. Flowfields

Figure 8 displays the flow structure of a typical two-dimensional jet-to-crossflow flowfield indicated by the Mach number distribution. The injected fuel expands into the main airflow, giving rise to a barrel shock wave, until it is terminated by a Mach disk. The freestream is obstructed by the barrel shock wave, causing a bow shock wave to stand upstream of the injection. The boundary layer is separated due to the presence of an adverse pressure gradient, inducing a large recirculation region, and subsequently a separation shock upstream of the injection.[16,29] The injected fuel flows in the horizontal direction downstream of the injection, with a recompression shock wave taking place farther downstream.

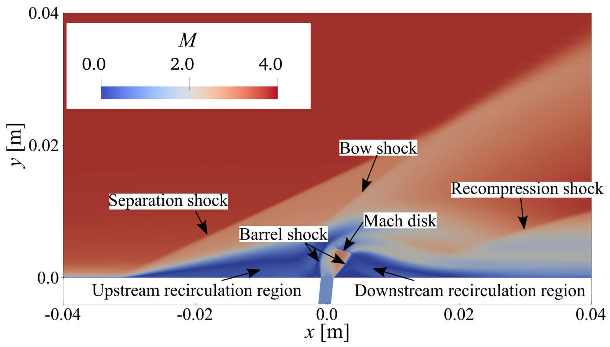


Fig. 8. Flow structure (Mach number distribution).

Compared in Fig. 9 are the true CFD and predicted MLP flowfields in terms of static pressure, static temperature, and helium mass fraction for an arbitrarily selected test case (i.e., ID 69, $p_j = 5.24 \times 10^4$ Pa, $\alpha_j = 84.2$ deg), but not used in the training of the MLP model. Good agreement is seen with respect to overall flow features such as shock waves and recirculation regions. Table 4 presents the RMSE and MAPE values for this case.

Figure 10 shows the absolute error distributions between the CFD result and the MLP prediction for the same case (i.e., ID 69). While the prediction is accurate in most regions, relatively large errors are found in the vicinity of the shock waves, the Mach disk, the boundary layer, and the boundary of the recirculation region. Difficulty in predicting abrupt changes in flow properties due to such phenomena can be attributed to the relatively small number of training data points (i.e., number of nodes) in these regions as compared to the

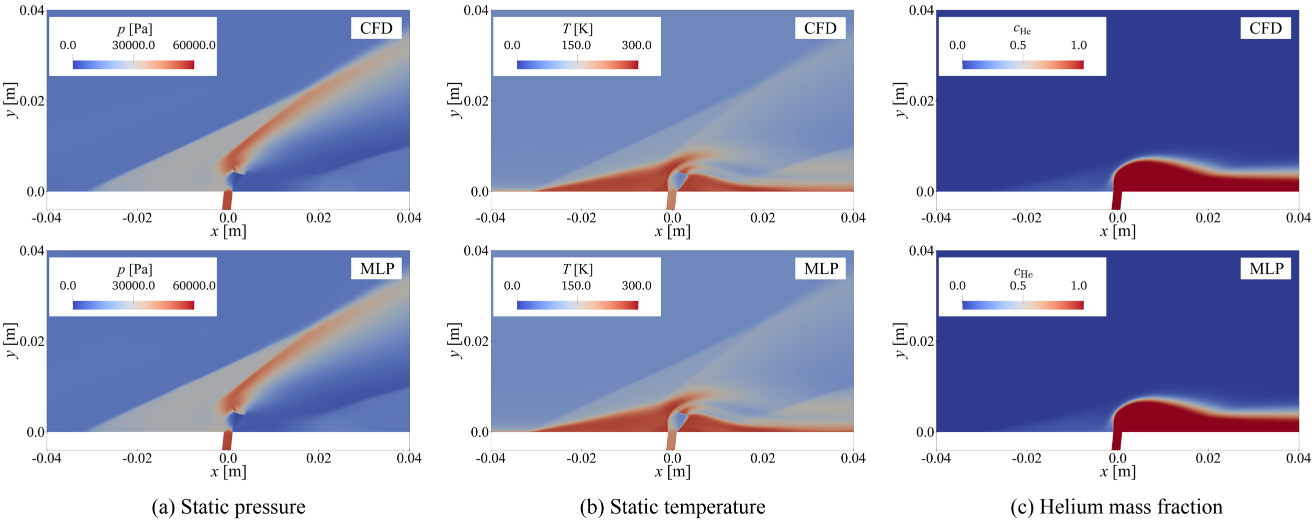


Fig. 9. Comparison of flow property distributions between CFD and MLP flowfields for the test case (ID 69, $p_j = 5.24 \times 10^4$ Pa, $\alpha_j = 84.2$ deg).

Table 4. RMSE and MAPE values for the test case (ID 69, $p_j = 5.24 \times 10^4$ Pa, $\alpha_j = 84.2$ deg).

| | $u$ [m/s] | $v$ [m/s] | $p$ [Pa] | $T$ [K] | $c_{He}$ | $c_{O_2}$ | $c_{N_2}$ |
|---|---|---|---|---|---|---|---|
| RMSE | 10.7 | 7.70 | 509 | 2.39 | $35.4 \times 10^{-4}$ | $8.82 \times 10^{-4}$ | $27.0 \times 10^{-4}$ |
| MAPE | $5.36 \times 10^6$ | $5.22 \times 10^6$ | $9.79 \times 10^{-3}$ | $6.51 \times 10^{-3}$ | 2.20 | 20.8 | 51.9 |

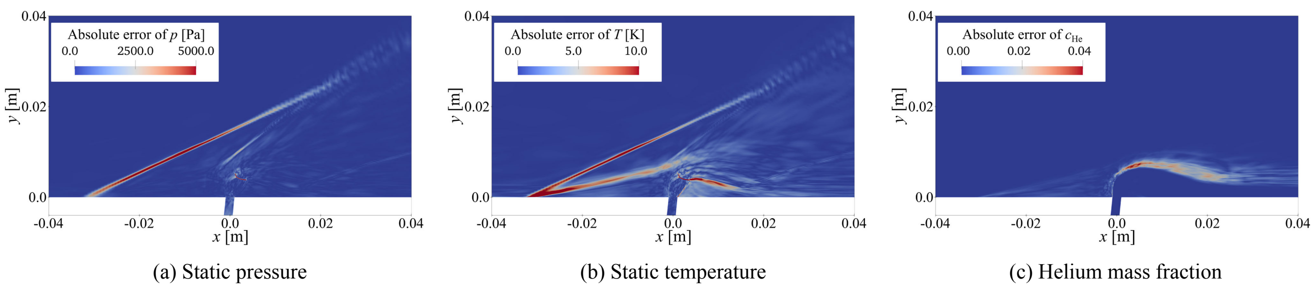


Fig. 10. Absolute error distributions between CFD and MLP flowfields for the test case (ID 69, $p_j = 5.24 \times 10^4$ Pa, $\alpha_j = 84.2$ deg).

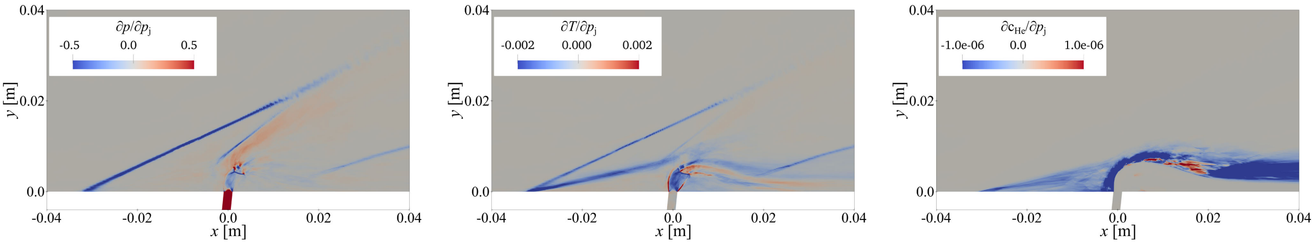


(a) Static pressure (b) Static temperature (c) Helium mass fraction

Fig. 11. Sensitivity of flow properties to injection pressure calculated from MLP (ID 69, $p_{\mathrm{j}} = 5.24 \times 10^{4}$ Pa, $\alpha_{\mathrm{j}} = 84.2$ deg).

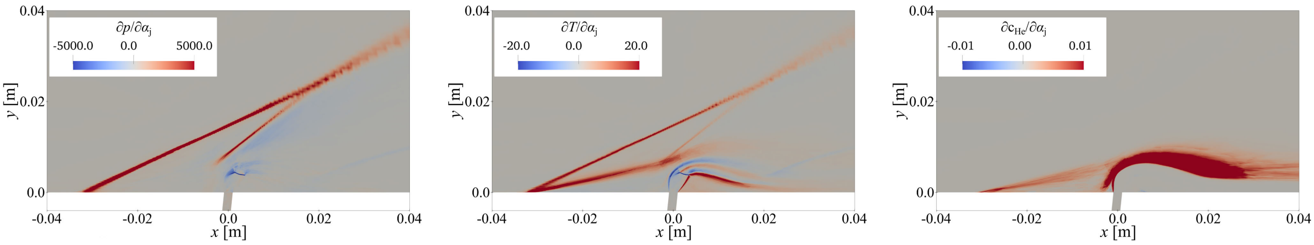


(a) Static pressure (b) Static temperature (c) Helium mass fraction

Fig. 12. Sensitivity of flow properties to injection angle calculated from MLP (ID 69, $p_{\mathrm{j}} = 5.24 \times 10^{4}$ Pa, $\alpha_{\mathrm{j}} = 84.2$ deg).

other regions with little or moderate changes (e.g., mainstream). Local mesh refinement and/or interpolation of data points may be considered to address the difficulty in such regions.

As for the computational cost, MLP training required approximately 10 h, which is equivalent to the calculation time of approximately five CFD simulations. On the other hand, flowfield prediction using the MLP model requires a fractional time of ~0.35 s once the model has been trained. This yields a substantial cost reduction, particularly for population-based design optimization which would inherently require a large number of objective function evaluations; hence CFD simulations otherwise.

### 3.3. Sensitivity analysis

Figures 11 and 12 display the variations of the sensitivity of the flow properties to the design variables for the configuration selected in Section 3.2 (i.e., ID 69, $p_{\mathrm{j}} = 5.24 \times 10^{4}$ Pa, $\alpha_{\mathrm{j}} = 84.2$ deg). Red and blue regions are indicative of large gradients (i.e., high sensitivity) in positive and negative directions, respectively, whereas gray regions indicate rather low sensitivity. It should be noted that the magnitude of the gradient or sensitivity to the injection pressure is significantly smaller than that to the injection angle owing to the wider variable range of the injection pressure; that is, 50,000 Pa $\leq p_{\mathrm{j}} \leq$ 200,000 Pa, as opposed to 30 deg $\leq \alpha_{\mathrm{j}} \leq$ 90 deg for the injection angle.

Negative gradient regions are found in static pressure and static temperature in the fuel plume (Figs. 11 (a) and (b), respectively), signifying that the degree of expansion of the injected fuel increases as injection pressure increases. In addition, a negative gradient is present in Figs. 11 (a) and (b) associated with the behavior of the separation point and the separation shock wave, which move downstream with the injection pressure. It should be noted that this behavior is opposed to the observations in previous studies where the separation point moved upstream with increasing injection pressure and injection angle.[4,29] Further, Fig. 11 (c) indicates that the helium mass fraction decreases in the upstream recirculation region and the mixing layer as injection pressure increases. This is because the injection width is decreased as the injection pressure increases to ensure the constant fuel mass flow rate in the present study, rendering the separation point move downstream in the present case (i.e., ID 69). Considerably low sensitivities of static pressure and static temperature in the fuel plume (Figs. 12 (a) and (b), respectively) are also indicative of rather little influence of the injection angle on the degree of fuel expansion. The separation shock wave moves upstream as the injection angle increases, which aligns with the observation reported in the previous study.[16]

Local sensitivity could also be obtained by performing CFD simulations and applying numerical differentiation to the resultant flowfields. The sensitivities of flow properties to injection pressure and angle calculated from CFD are displayed for comparison in Figs. 13 and 14, respectively, exhibiting similar tendencies to those from MLP (Figs. 11 and 12). This validates the local sensitivity from MLP, which can calculate the sensitivity of the design variables within 1 s in stark contrast to CFD, which takes about 2 h. This enables cost-effective, robust design exploration that considers the variations of performance associated with local flow phenomena against deviations in the design variables or conditions.

### 3.4. Prediction error

To probe the prediction behavior associated with large prediction errors, the static pressure distributions are compared between the CFD and MLP flowfields in Fig. 15 for the case with the largest RMSEs of static pressure (i.e., ID

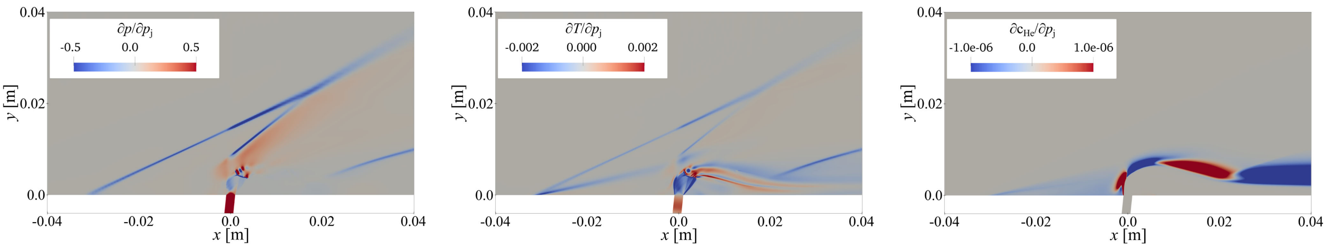


(a) Static pressure (b) Static temperature (c) Helium mass fraction

Fig. 13. Sensitivity of flow properties to injection pressure calculated from CFD (ID 69, $p_\mathrm{j} = 5.24 \times 10^4$ Pa, $\alpha_\mathrm{j} = 84.2$ deg).

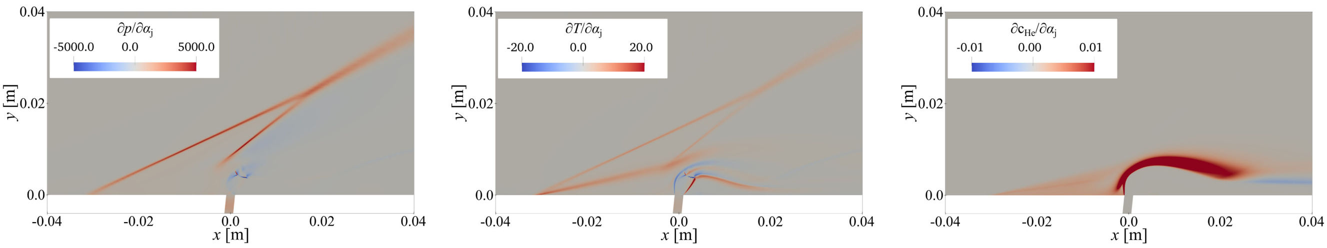


(a) Static pressure (b) Static temperature (c) Helium mass fraction

Fig. 14. Sensitivity of flow properties to injection angle calculated from CFD (ID 69, $p_\mathrm{j} = 5.24 \times 10^4$ Pa, $\alpha_\mathrm{j} = 84.2$ deg).

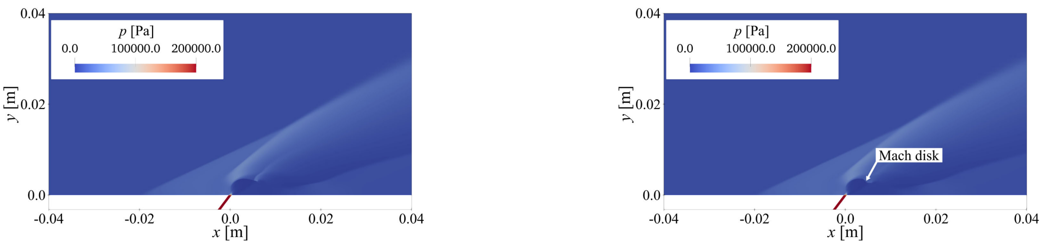


(a) CFD (b) MLP

Fig. 15. Comparison of static pressure between CFD and MLP flowfields (ID 274, $p_\mathrm{j} = 1.99 \times 10^5$ Pa, $\alpha_\mathrm{j} = 52.9$ deg).

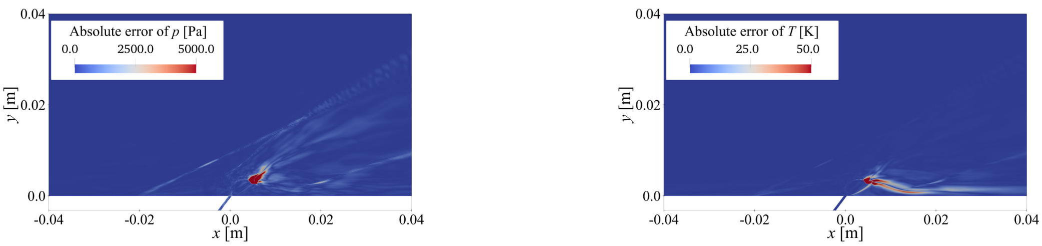


(a) Static pressure (b) Static temperature

Fig. 16. Absolute error distributions of static pressure and static temperature between CFD and MLP flowfields (ID 274, $p_\mathrm{j} = 1.99 \times 10^5$ Pa, $\alpha_\mathrm{j} = 52.9$ deg).

274, $p_\mathrm{j} = 1.99 \times 10^5$ Pa, $\alpha_\mathrm{j} = 52.9$ deg). The absolute error distributions of static pressure and static temperature are shown in Fig. 16. While the prediction is accurate in most regions including the vicinity of the separation shock wave, relatively large absolute errors in static pressure and static temperature are observed near the Mach disk. This is associated with the absence of a Mach disk at the downstream end of the barrel shock in the CFD result in Fig. 15 (a), whereas the barrel shock in the flowfield predicted by MLP is characterized by the presence of a discernible Mach disk in Fig. 15 (b).

Table 5. Design variables for the selected cases.

| ID | $p_\mathrm{j}$ [Pa] | $\alpha_\mathrm{j}$ [deg] |
|---|---|---|
| 74 | $1.81 \times 10^5$ | 54.7 |
| 78 | $1.97 \times 10^5$ | 63.4 |
| 272 | $1.95 \times 10^5$ | 50.3 |

Three cases shown in Table 5 have been selected from the dataset used for training as neighboring instances to the case with the largest prediction error (i.e., ID 274) in the design space to probe the factors that account for large errors. The

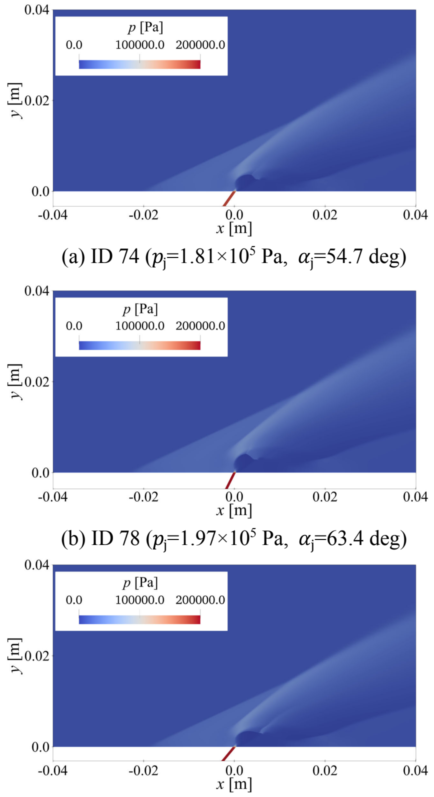


(a) ID 74 ($p_j$=1.81×10$^5$ Pa, $\alpha_j$=54.7 deg)

(b) ID 78 ($p_j$=1.97×10$^5$ Pa, $\alpha_j$=63.4 deg)

(c) ID 272 ($p_j$=1.95×10$^5$ Pa, $\alpha_j$=50.3 deg)

Fig. 17. Static pressure distributions calculated from CFD for the selected cases.

static pressure distributions calculated from CFD are compared in Fig. 17. In ID 74 ($p_j = 1.81 \times 10^5$ Pa, $\alpha_j = 54.7$ deg) and ID 78 ($p_j = 1.97 \times 10^5$ Pa, $\alpha_j = 63.4$ deg). A Mach disk stands perpendicularly to the barrel shock wave, akin to that shown in Fig. 15 (b), whereas the barrel shock is characterized by a pointed tip without a Mach disk in ID 272 ($p_j = 1.95 \times 10^5$ Pa, $\alpha_j = 50.3$ deg), similar to the case shown in Fig. 15 (a). This signifies that the existence of the Mach disk has changed sensitively to rather little variation in the design variables in this region. This again underpins the difficulty in training and prediction for regions subjected to abrupt changes in flow properties.

## 4. Conclusions

The applicability of deep learning to jet-to-crossflow flowfields has been investigated, aiming at fast prediction of compressible flowfields to be incorporated into data-driven design approaches for high-speed aerospace applications. Two-dimensional flowfields with sonic fuel injection into a supersonic crossflow defined by two design variables, namely fuel injection pressure and angle, have been trained using MLP.

The trained model was found to be able to accurately predict flowfields even for instances that have not been used for training. Local sensitivity analysis was conducted to examine the influence of the design variables on local flow phenomena. It was demonstrated that the sensitivity of the flow properties to the design variables can be quantified at low computational cost once the MLP model has been trained. The results of the sensitivity analysis indicated that the flow properties are sensitive to the design variables near the shock waves, in recirculation regions, and downstream of the injection. Further, the fuel mass fraction in the upstream recirculation region was found to change sensitively to variation in design variables. In the flowfield of the case with the largest root mean squared error, considerably large prediction errors were observed near the Mach disk, whose existence was found to be sensitive to the variation in design variables.

The insights gained from this study will contribute to developing and utilizing deep learning approaches for design and optimization of aerospace applications that involve complex compressible phenomena. Further investigation on the potential of this MLP model incorporated into multi-objective design optimization is a subject of future work. Additionally, its ability to predict higher dimensional flowfields for configurations with a larger number of design variables will be assessed.

## Acknowledgments

The authors acknowledge the support provided by the Japan Society for the Promotion of Science through JSPS KAKENHI Grant Number JP 17K20144.

## References

1) McClinton, C. R.: X-43–Scramjet Power Breaks the Hypersonic Barrier Dryden Lectureship in Research for 2006, AIAA Paper 2006-0001, 2006.
2) Smart, M. K., Hass, N. H., and Paull, A.: Flight Data Analysis of the HyShot 2 Scramjet Flight Experiment, *AIAA J.*, **44** (2006), pp. 2366–2375.
3) Erdem, E. and Kotis, K.: Numerical and Experimental Investigation of Transverse Injection Flow, *Shock Waves*, **20** (2010), pp. 103–118.
4) Wang, Z., Jiang, C., Gau, Z., and Lee, C.: Prediction for the Separation Length of Two-Dimensional Sonic Injection with High-Speed Crossflow, *AIAA J.*, **55** (2017), pp. 832–847.
5) Huang, W., Liu, W., Li, S., Xia, Z., Liu, J., and Wang, Z.: Influence of the Turbulence Mode and the Slot Width on the Transverse Slot Injection Flow Field in Supersonic Flows, *Acta Astronaut.*, **73** (2012), pp. 1–9.
6) Ogawa, H.: Effects of Injection Angle and Pressure on Mixing Performance of Fuel Injection via Various Geometries for Upstream-fuel-injected Scramjets, *Acta Astronaut.*, **128** (2016), pp. 485–498.
7) Ogawa, H. and Boyce, R. R.: Physical Insight into Scramjet Inlet Behavior via Multi-Objective Design Optimization, *AIAA J.*, **50** (2012), pp. 1773–1783.
8) Fujio, C. and Ogawa, H.: Physical Insight into Axisymmetric Scramjet Intake Design via Multi-objective Design Optimization Using Surrogate-assisted Evolutionary Algorithms, *Aeros. Sci. Technol.*, **113** (2021), 106676.
9) Du, J., Fang, F., Pain, C. C., Navon, I. M., Zhu, J., and Ham, D. A.: POD Reduced-order Unstructured Mesh Modeling Applied to 2D and 3D Fluid Flow, *Comput. Math. Appl.*, **65** (2013), pp. 362–379.
10) Schmid, P. J.: Dynamic Mode Decomposition of Numerical and Experimental Data, *J. Fluid Mech.*, **656** (2010), pp. 5–28.
11) Ströfer, C. M., Wu, J., Xiao, H., and Paterson, E.: Data-Drive, Physics-Based Feature Extraction from Fluid Flow Fields, *Commun. Comput. Phys.*, **25** (2019), pp. 625–650.
12) Raissi, M., Perdikaris, P., and Karniadakis, G. E.: Physics-informed Neural Networks: A Deep Learning Framework for Solving Forward and Inverse Problems Involving Nonlinear Partial Differential Equa-

tions, *J. Comput. Phys.*, **378** (2019), pp. 686–707.
13) Rao, C., Sun, H., and Liu, Y.: Physics-informed Deep Learning for Incompressible Laminar Flows, *Theor. Appl. Mech. Lett.*, **10** (2020), pp. 207–212.
14) Sekar, V., Jiang, Q., Shu, C., and Khoo, B. C.: Fast Flow Field Prediction over Airfoils Using Deep Learning Approach, *Phys. Fluids*, **31** (2019), 057103.
15) Kong, C., Chang, J., Li, Y., and Wang, Z.: A Deep Learning Approach for the Velocity Field Prediction in a Scramjet Isolator, *Phys. Fluids*, **33** (2021), 026103.
16) Inoue, K., Aso, S., and Kawano, S.: A Study on the Effect of Fuel Injection Angle to Two-Dimensional Supersonic Mixing for SCRAM-Jet engine and PDE, 54th International Astronautical Congress of the International Astronautical Federation, the International Academy of Astronautics, and the International Institute of Space Law, Bremen, Germany, 2003, pp. 1–9.
17) ANSYS Fluent User's Guide, Ver. 2021 R1, ANSYS Inc., Canonsburg, PA, 2021.
18) Liou, M.-S. and Steffen, C. J., Jr.: A New Flux Splitting Scheme, *J. Comput. Phys.*, **107** (1993), pp. 23–39.
19) Menter, F. R.: Two-Equation Eddy-Viscosity Turbulence Models for Engineering Applications, *AIAA J.*, **32** (1994), pp. 1598–1605.
20) Geuzaine, C.: Gmsh: A 3-D Finite Element Mesh Generator with Builtin Pre- and Post-processing Facilities, *Int. J. Numer. Methods Eng.*, **79** (2009), pp. 1309–1331.
21) Abadi, M., Agarwal, A., Barham, P., Brevdo, E., Chen, Z., Citro, C., Corrado, G. S., Devis, A., Dean, J., Devin, M., Chemawat, S., Goodfellow, I., Harp, A., Irving, G., Isard, M., Jia, Y., Jozefowicz, R., Kaiser, L., Kudlur, M., Levenberg, J., Mané, D., Monga, R., Moore, S., Murray, D., Olah, C., Schuster, M., Shlens, J., Seiner, B., Sutskever, I., Talwar, K., Tuker, P., Vanhoucke, V., Vasudevan, V., Viégas, F., Vinyals, O., Warden, P., Wattenberg, M., Wicke, M., Yu, Y., and Zheng, X.: TensorFlow: Large-scale Machine Learning on Heterogeneous Systems, Software available from https://www.tensorflow.org, 2015.
22) LeCun, Y., Bengio, Y., and Hinton, G.: Deep Learning, *Nature*, **521** (2015), pp. 436–444.
23) Stein, M.: Large Sample Properties of Simulations Using Latin Hypercube Sampling, *Technometrics*, **29** (1987), pp. 143–151.
24) Kingma, D. P. and Ba, J.: Adam: A Method for Stochastic Optimization, 3rd International Conference on Learning Representations, 2015, pp. 1–15.
25) Vellido, A.: The Importance of Interpretability and Visualization in Machine Learning for Applications in Medicine and Health Care, *Neural. Comput. Appl.*, **32** (2020), pp. 18069–18083.
26) Roscher, R., Bohn, B., Duarte, M. F., and Garcke, J.: Explainable Machine Learning for Scientific Insights and Discoveries, *IEEE Access*, **8** (2020), pp. 42200–42216.
27) Simonyan, K., Vedaldi, A., and Zisserman, A.: Deep Inside Convolutional Networks: Visualising Image Classification Models and Saliency Maps, Workshop at International Conference on Learning Representations, 2014, pp. 1–8.
28) Baydin, A. G., Pearlmutter, B. A., Radul, A. A., and Siskind, J. M.: Automatic Differentiation in Machine Learning: a Survey, *J. Mach. Learn Res.*, **18** (2018), pp. 1–43.
29) Aso, S., Okuyama, S., Kawai, M., and Ando, Y.: Experimental Study on Mixing Phenomena in Supersonic Flows with Slot Injection, AIAA Paper 91-0016, 1991.

Nobuyuki Tsuboi
*Associate Editor*